SPECTROSCOPIC METHODOLOGY – Full Papers

Magnetic Resonance in Medicine 73:901–908 (2015)

Fast Low-Specific Absorption Rate B_0-Mapping along Projections at High Field Using Two-Dimensional Radiofrequency Pulses

Olivier Reynaud,* Daniel Gallichan, Benoit Schaller, and Rolf Gruetter

Purpose: At 7 Tesla (T), conventional static field (B_0) projection mapping techniques, e.g., FASTMAP, FASTESTMAP, lead to elevated specific absorption rates (SAR), requiring longer total acquisition times (TA). In this work, the series of adiabatic pulses needed for slab selection in FASTMAP is replaced by a single two-dimensional radiofrequency (2D-RF) pulse to minimize TA while ensuring equal shimming performance.

Methods: Spiral gradients and 2D-RF pulses were designed to excite thin slabs in the small tip angle regime. The corresponding selection profile was characterized in phantoms and in vivo. After optimization of the shimming protocol, the spectral linewidths obtained after 2D localized shimming were compared with conventional techniques and published values from (Emir et al NMR Biomed 2012;25:152–160) in six different brain regions.

Results: Results on healthy volunteers show no significant difference ($P > 0.5$) between the spectroscopic linewidths obtained with the adiabatic (TA = 4 min) and the new low-SAR and time-efficient FASTMAP sequence (TA = 42 s). The SAR can be reduced by three orders of magnitude and TA accelerated six times without impact on the shimming performances or quality of the resulting spectra.

Conclusion: Multidimensional pulses can be used to minimize the RF energy and time spent for automated shimming using projection mapping at high field. **Magn Reson Med 73:901–908, 2015. © 2014 Wiley Periodicals, Inc.**

Key words: FASTMAP; FASTESTMAP; projection mapping; spiral; 2D-RF pulse; SAR

INTRODUCTION

High resolution MR spectroscopy (MRS) benefits from the use of higher field-strength through the broader spectral dispersion and sensitivity increase (1,2). Adjustment of the static field, or B_0 shimming, is especially important as it defines the spectral resolution, hence, the capability to separate between neighboring metabolite resonances. Cautious magnetic field shimming relies on an iterative process consisting of: B_0 field characterization (or field mapping) and compensation by adapting the power of shim coils (3,4).

Field mapping methods can be split in two groups—3D B_0 mapping (5–7) and projection mapping (8–12). The 3D techniques assess B_0 in each voxel. They are frequently used for MRI or MR spectroscopic imaging (MRSI), both requiring good B_0 homogeneity over a large field of view (FOV). On the other hand, projection mapping techniques only use a few orientations to compute the spherical harmonics components of the local B_0 field (9). Because local variations are easily compensated by first- and second-order shims, these methods result in a considerable gain of time compared with three-dimensional (3D) acquisitions, six directions being sufficient to characterize B_0 up to the second order with high spatial sampling. Local fields can be rapidly characterized with high accuracy, making projection mapping a widely used technique in single voxel MRS (13).

In both methods, field mapping is performed by acquiring at least two datasets with distinct echo times (TE). The phase accumulated during the TE difference is proportional to the local B_0 field. Using multiple TEs after a single excitation allows for fast B_0 mapping over a large scale range of inhomogeneities. By combining projection mapping and multiple read-outs, FASTESTMAP (10) can provide efficient multiscale B_0 field characterization.

Historically, FASTMAP and its derivative techniques (8–12) have incorporated more and more adiabatic radiofrequency pulses to compensate for the increased B_1 field inhomogeneity at high field. Its most recent implementation consists of one $\pi/4$ and four π adiabatic pulses (10). The drawback to this robustness against B_1 inhomogeneity is an increased RF energy, making the technique less suitable for rapid field mapping. Specific absorption rate (SAR) limitations lead indeed to elevated repetition times (TR) and restrain the potential of FASTMAP and FASTESTMAP at high field.

The aim of the present study was to replace the series of adiabatic pulses needed for columnar/cylindrical selection by a single 2D-RF pulse and to compare the performance of the resulting technique with literature values and with the presently implemented method.

METHODS

All of the experiments were performed on a Siemens 7 Tesla (T) / 68 cm head scanner (Siemens Healthcare, Erlangen, Germany) using a single-channel quadrature transmit and 32-channel receive coil array (Nova Medical Inc., Wilmington, MA). A 16 cm diameter sphere filled with water + 0.8% sodium acetate (Na, $C_2H_3O_2$) and 1% formaldehyde (Li, $C_3H_5O_3$) was used for experimental profile characterization.

CIBM, EPFL, Lausanne, Switzerland.

*Correspondence to: Olivier Reynaud, Ph.D., LIFMET, EPFL, Lausanne, Station 6, CH-1015, Lausanne, Switzerland. E-mail: oli.reynaud@gmail.com

Received 13 December 2013; revised 13 February 2014; accepted 13 February 2014

DOI 10.1002/mrm.25217

Published online 10 April 2014 in Wiley Online Library (wileyonlinelibrary.com).

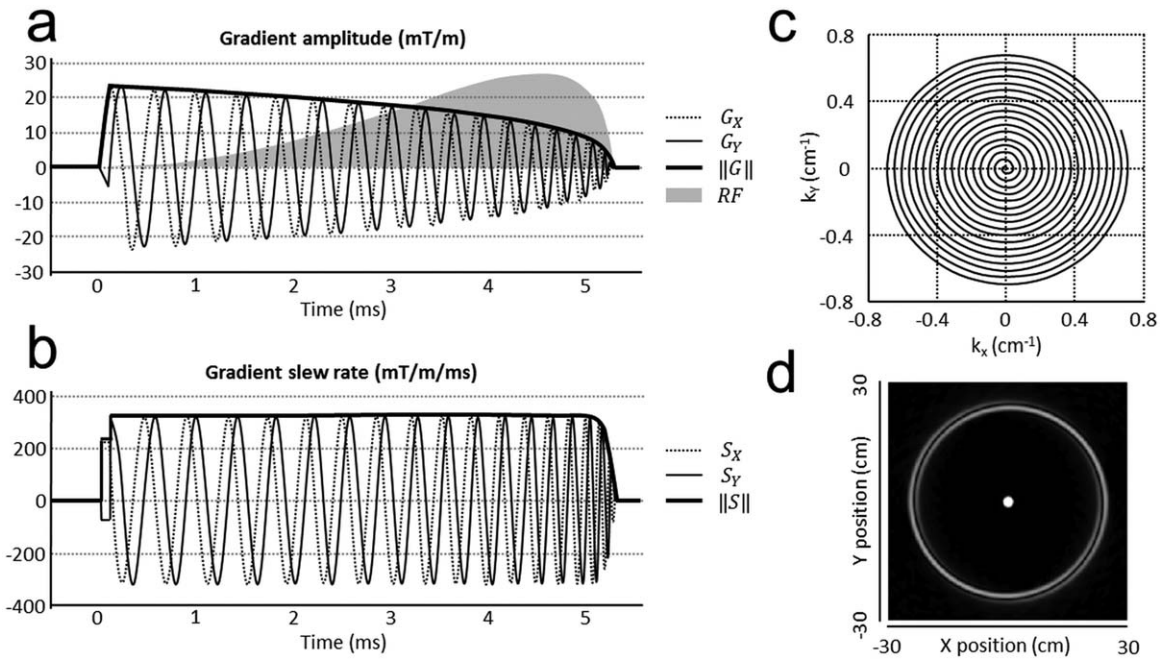

FIG. 1. **a:** Spiral-in gradient waveform (5.17 ms) generated using an exponential slew-rate recovery model (20) and RF shape (gray area, arbitrary units) exciting a 0.7-cm cylinder radius. **b:** Following hardware limitations, the gradient time-derivative shows that the gradient system is working in the slew-rate limited regime (330 mT/m/ms), and further constrained near the k-space center. **c:** Corresponding excitation k-space. The maximum extent in k-space k_{max} and the interval between two consecutive spiral turns characterize the cylinder radius and position of the first aliasing lobes of the excitation profile. **d:** The simulated excitation profile (FA = 30°, FOV 30 × 30 cm^2, arbitrary units).

Gradient Waveform and RF Pulse Design

The objective was to design a single 2D-RF pulse for moderate excitation (flip angle: FA < 45°) of a small "pencil" 2D profile at 7T. B_0 variations induce spins dephasing and introduce distortions and blurring in the profile of long multidimensional RF pulses (14,15). As a result, pulse durations and gradient trajectories were kept as short as possible. The efficient k-space coverage of the spiral trajectory ensured minimization of the pulse shape duration (16,17).

Given the cubic shimming voxel size, a, the desired radius, r_0, of the excited cylinder was determined using the empiric "rule of thumb" formula: $r_0 = a\sqrt{2}/6$ (8). This threshold ensured that the slab was thin enough so that the phase difference measured between two projections was dominated by the variations along the cylinder, and phase variations perpendicular to each cylinder could be neglected. Aliasing lobes inherent to spiral trajectories (18,19) were pushed far outside the brain by setting their location r_1 at 24 cm. The other spiral parameters, such as number of spiral turns $N_{spirals}$ and extent in k-space k_{max} (in cm^{-1}), were then derived from r_0 and r_1 (in cm) using $k_{max} = 1/(2r_0)$ and $N_{spirals} = r_1/2r_0$.

Following hardware constraints (maximum gradient strength 80 mT.m^{-1}, maximum slew-rate 330 mT.m^{-1}.ms^{-1}), spiral-in gradient waveforms using exponential (20) and polynomial slew-rate recovery (21) around the k-space origin were designed and compared with the linear gradient waveform described by Ahn et al and Pauly et al (22–24).

The gradient waveforms were calculated with a 10 μs time interval to match the raster-time of the waveform generator and the k-space trajectory was resampled onto a 1 μs raster to meet the dwell-time of the RF amplifier. As in Pauly et al (23), the RF pulse was shaped as the Fourier Transform of a circle of radius r_0. The resulting first-order Bessel function, possessing a single zero-crossing in k_{max}, was convolved—for apodization—with a radially Gaussian function. The resulting shape was then weighted by the k-space density compensation function (18). The radially monotonous behavior of the spiral trajectory and desired profile led to slowly varying RF pulse shapes, as illustrated in Figure 1a.

RF Energy Deposition

Energy depositions of the adiabatic RF (E_{AD}) and 2D-RF (E_{2D}) pulse versions of FASTMAP/FASTESTMAP were calculated and compared for various projection radii (0.7–2 cm) in our range of interest for MRS (voxel size: 3.0–8.5 cm). TR and FA were kept identical to the values used in the full adiabatic implementation of the sequence (FA = 45°, TR = 3000 ms). The relative SAR (rSAR, in %) of the 2D-RF pulses was computed using the following formula: $rSAR = 100 * E_{2D}/E_{AD}$.

Total Acquisition Time

In addition to the reduced energy deposition, and therefore minimum available TR, using a 2D-RF pulse offers a third advantage in terms of reduced TE. With spiral-in gradients, the center of excitation k-space is reached at the end of the gradient waveform. TE is then only constrained by the read-out defocusing gradient duration

Table 1
Full Protocol for Localized Shimming at 7T

# Iterations	Type of sequence	Projections	ΔTE (ms)	Shims
x 1	FASTMAP	X,Y,Z	2.0	1st order
x 1	FASTMAP	XY,YX,XZ,ZX,YZ,ZY	4.0	1st order
x 1	FASTMAP	XY,YX,XZ,ZX,YZ,ZY	6.0	1st order
x 3	FASTMAP	XY,YX,XZ,ZX,YZ,ZY	8.0	1st order
x 2	FASTESTMAP	XY,YX,XZ,ZX,YZ,ZY	6.3/12.6/18.9/25.2/31.5/37.8	2nd order

and half of the acquisition period. In this study, reducing TE from 31 to 5 ms was used to reduce both TR and FA, to the Ernst angle $FA_{Ernst} = \text{acos}(\exp(-TR/T_1))$, while keeping a signal level similar to that of the initial sequence.

Based on the T_1 of gray matter at 7T (25) ($T_{1GM} = 1.9$ s), the GE MR signal was simulated for several values of TR (100–3000 ms) and corresponding FA_{Ernst}. TR was then minimized while a signal level equal to that of the adiabatic implementation of the method was maintained.

Gradient System Calibration and Excitation Profile

Despite gradient system pre-emphasis adjustment, non-negligible eddy currents can remain and be amplified by the intensive gradient slew-rate. It has been shown that eddy currents can be considered in a first approximation as delays between two gradients, or between gradients and the RF pulse shape (18). As in Davies and Jezzard and Robison et al (26,27), additional delays were implemented to compensate for such effects.

2D-RF pulses were used as excitation pulses on a 3D gradient-echo (GE) sequence to visualize the full spatial profile of the cylinder (radius 0.7 cm, pulse duration 5.17 ms). The 3D-GE parameters were: TR/TE = 500/5 ms, FOV 200 × 200 × 192 mm^3, matrix size 256 × 256 × 32. The cylinder was shifted to the position (x_0, y_0) by modulating the 2D-RF pulse phase by the instantaneous frequency $\omega(t) = k_x(t).x_0 + k_y(t).y_0$, where $k_x(t)$ and $k_y(t)$ represent the temporal positions inside the excitation k-space, corresponding to gradients waveforms along axes X and Y, respectively. As in Davies and Jezzard (26), delays between the X and Y gradients and the RF pulse shape were then adjusted manually on a 1 μs scale to minimize profile distortions and errors between the experimental and theoretical excitation locations, defined by (x0,y0) = [(0,50), (0,−50), (50,0), (−50,0)] mm. The experiment was repeated with a different orientation to adjust the delay between the 2D-RF pulse shape and the Z gradient.

To characterize the experimental excitation profile at high resolution, the 2D-RF pulses were implemented as excitation pulses on a single slice Spin-Echo (SE) sequence, as in Pauly et al (23). The following MR parameters ensured sufficient SNR: TR/TE = 500/15 ms, FOV = 192 × 192 mm^2, slice thickness = 10 mm, matrix size 128 × 128, NA = 20, TA = 17 min 20 s. After the 2D excitation, spins were refocused in a 10 mm plane orthogonal to the slab. The experimental profile of the 2D-RF pulse previously designed was first characterized on a spherical phantom by measuring its full width at half maximum (FWHM) for various FA between 5 and 90°. The optimal FA was adjusted to ensure compliance to the small tip angle approximation and good spatial selectivity. The experimental profile was then characterized in vivo (occipital cortex, slab orientation = YZ) after global shimming and compared with simulations in a perfect medium, after estimation of the Cayley-Klein parameters for the rotation introduced by the RF pulse (28).

Shimming Process

In practice, a full shimming process requires several iterations of projection mapping with different phase evolution times ΔTE. Typically, first-order shims (X, Y, Z) compensate for large B_0 perturbations fitted with a small ΔTE (on the order of 2 ms at 7T) that cannot be accessed using multiple echo sequences, such as FASTESTMAP (10). The evolution time is increased and the static field further adjusted in the range ΔTE ∈ [2–8] ms by successive iterations of: mapping along six projections followed by first-order shim-compensation (8). Residual B_0 variations can be easily mapped in a short amount of time using only a few FASTESTMAP iterations, each probing six different ΔTE values in the range [6–38] ms. A very conservative protocol was used here to show the algorithm convergence in various brain regions. The full localized shimming process used at 7T in (1,29) is detailed in Table 1. The final quality of B_0 shimming is assessed by calculating the average water spectral linewidth inside the volume of interest (VOI).

In Vivo MR Protocol

For in vivo validation at 7T, the new shimming algorithm was tested in the brain of 14 healthy subjects (age 21 to 35). Volunteers gave informed consent according to a procedure approved by local ethics committee. Two dielectric pads (D_2O + 20 % BaO_3,Ti) were placed around the subject's head near the occipital lobe and the left hemisphere to enhance the local B_1 field coverage in the regions of interest (30,31). Six VOIs were delineated (occipital cortex, frontal white matter, posterior cingulate, putamen, substantia nigra, and cerebellum) to cover regions across most of the human brain. The VOI was adapted to the size of the anatomical structure, with the volume varying between 1 mL (substantia nigra) and 8 mL (occipital cortex, frontal white matter, posterior cingulate).

After global shimming using standard 3D B_0 field mapping, anatomical images were acquired using a two echo-

train version of the magnetization prepared rapid GE sequence (MP2RAGE (25)). The MR imaging parameters were as follows: TR/TE = 6000/2.82 ms, TI_1/TI_2 = 800/2700 ms, FA_1/FA_2 = 4/5 °, FOV = 256 × 256 × 160 mm^3, res. 1 mm isotropic, TA = 8 min 8 s. An additional SA2RAGE scan (32) (TR/TE = 2400/1.41 ms, TI_1/TI_2 = 65/1800 ms, FA_1/FA_2 = 4/11 °, FOV 256 × 256 × 196, res. 2 × 2 × 2.5 mm^3, TA = 2 min 23 s) was performed for B_1 correction of the T_1 map and RF power calibration in the different shimming VOIs.

The precise location and RF power required in each VOI were assessed using the MP2RAGE "flat" images and the SA2RAGE B_1+ maps, respectively. Localized shimming was then performed in 25 × 25 × 25 mm^3 volumes with the optimized 2D-RF excitation pulses (FA = 25°, radius r_0 = 0.7 cm) and FASTMAP/FASTESTMAP according to the protocol detailed in Table 1 (TR/TE = 500/5 ms, TA = 42 s). The water spectral linewidths values $FWHM_{H2O}$ were derived from the free induction decay (FID) obtained with a STEAM sequence (33) (TR/TE = 4000/15 ms, SW = 2000 Hz, vector size = 4096, 4 preparation scans, VOI = 20 × 20 × 20 mm^3, TA = 20 s). After Fourier transformation and phase correction, the linewidth ($FWHM_{H2O}$, in Hz) of the water spectrum was measured.

The difference between the water spectral linewidths obtained in the occipital cortex with the AD-RF and the 2D-RF versions of the localized shimming method was tested for statistical significance (N = 7). The two-sample paired student t-test was used to calculate the probability (*P*) value that the two resulting $FWHM_{H2O}$ values were equal.

In all six VOIs (seven subjects per ROI, total of nine subjects) the results obtained after 2D-RF shimming were also compared with the literature on localized shimming at 7T (1,34–37). In particular, Emir et al (34) was used for reference (mean ± standard deviation of $FWHM_{H2O,ref}$ in each VOI). A two-tailed Welch t-test (unequal sample size and variance) was used to test the null hypothesis that the two population means $FWHM_{H2O}$ and $FWHM_{H2O,ref}$ were different. For both tests, a *P*-value $P < 0.05$ was regarded as significant.

The neurochemical profile was quantified in the posterior cingulate of one additional subject to illustrate the good quality of the spectra acquired after 2D-RF localized shimming. The proton spectrum was acquired with a semi-adiabatic SPECIAL localization sequence (38) (TR/TE = 7500/12 ms, BW = 4000 Hz, 2048 points, RF pulse frequency offset = 2.3 ppm, NA = 32, TA = 4 min). VAPOR water suppression (WS) was interleaved with blocks of outer volume saturation (OVS) to minimize the unwanted water and lipid contamination (13,29). The spectrum was fitted and quantified with LCModel (39) using a basis set including simulated spectra of 20 metabolites with published values for chemical shift and J-coupling (40,41). The macromolecule baseline was measured experimentally. The LCModel analyses were carried out from 0.2 ppm to 4.2 ppm. We used the Cramer-Rao lower bound (CRLB) as a marker of quantification reliability (39,42). Metabolites with CRLBs below 20 % were considered to be unambiguously identified and quantified.

RESULTS

Gradient Trajectory

To shim a 30 × 30 × 30 mm^3 voxel (common size for MRS), spiral gradient waveforms and pulse shape were designed to excite a slab with radius r_0 = 0.7 cm inside that cube. The different gradient durations found by using the exponential, polynomial, or linear slew-rate design approach were 5.17 ms, 5.25 ms, and 7.68 ms, respectively. As expected, the methods proposed by Zhao et al (20) and Glover (21), working at maximum performance except at the vicinity of the k-space center, showed a substantial gain of time compared with the constant linear velocity spiral trajectory (22,23). As in Nehrke et al (18), we chose Zhao's exponential time constant τ = 50 μs, the smallest multiple of the gradient dwell time (10 μs) that would not cause a slew rate overshoot near the center of k-space, resulting in the 5.17-ms-long spiral gradient waveforms (Fig. 1a), with corresponding gradient slew-rates and excitation k-space coverage (Figs. 1b and 1c), respectively. The expected profile for a 0.7 cm radius cylindrical excitation and flip angle of 30° (Fig. 1d) showed that the first aliasing lobe radius exceeded by far the brain dimensions.

RF Energy Deposition

For cylinder radii in the range [0.7–2.0] cm, we found rSAR values in the range [0.02–0.11] % between a single 2D-RF pulse and the five adiabatic RF pulses used for projection mapping (i.e., 900 to 5000 times lower SAR). Based on this dramatic reduction in overall RF power deposition, the choice of TR was no longer limited by SAR, and could be reduced well below 3000 ms to decrease the overall time needed for shimming.

Reduction of Total Acquisition Time

Using a single 2D-RF pulse allowed a significant reduction of TE from 31 to 5 ms, resulting in a 225 % SNR increase in gray matter. TR = 500 ms (and FA = FA_{Ernst} = 40°) were found sufficient to obtain a signal level equivalent to that of the full AD implementation, as seen in Table 2. As a result, only 6 and 3 s were needed to acquire six projections with FASTMAP and FASTESTMAP. Based on these parameters, the total time needed for shimming was decreased by 83% per iteration without any signal loss (see Table 2). Using adiabatic versus 2D-RF pulses the total shimming durations (according to the protocol detailed in Table 1) were 237 s versus 42 s, respectively. These included the 3000 ms settling times required by the hardware when modifying second-order shim currents.

Experimental Excitation Profile

The experimental profiles generated in a spherical phantom (see Fig. 2a) by 30° 2D-RF pulses whose long axes were oriented along XY or Z are illustrated in Figure 2b and 2c (coronal planes). As seen in Figure 2c, the excitation profiles in slices orthogonal to the cylinder axis were well localized on the different axes and did not require the implementation of extra delays between the

Table 2
Total Acquisition Time Required for B_0 Mapping along Six Projections Using FASTMAP/FASTESTMAP and Three Set of Excitation Parameters

RF Pulse	TR (ms)	FA (°)	rSAR (%)	m_{SS}[a] (%)	$TA_{FASTMAP,6p}$ (s)	$TA_{FASTESTMAP,6p}$ (s)
AD	3000	45	100	–	36	18
2D #1	500	40	0.2	100	6	3
2D #2	500	25	0.07	91	6	3

[a]The steady state GE MR signal at TE = 5 ms was normalized to the MR signal of the full-AD technique used in routine at 7T (TR = 3000 ms, FA = 45°, TE = 31 ms).

RF and the different gradient waveforms. These results were found to be reproducible and independent of the radius and slab orientation (data not shown). This suggested a good pre-emphasis system calibration and little evidence of eddy currents effects, even at maximum slew-rate.

Experimentally, the FWHM of the $r_0 = 0.7$ cm slabs were measured for various FA values. The results (FWHM $\in$ [1.4–2.3] cm for FA $\in$ [5–90]°) showed good agreement between the theoretical and experimental spatial profiles for small FA 2D-RF pulses (FA $<$ 30°). Because the optimal FA was estimated around 40° and our 2D-RF pulse design based on the small tip angle approximation, the true FWHM of the slab was likely to exceed its nominal value. Our simulations showed that the theoretical GE signal level at TR = 500 ms did not vary much ($<$ 10 %) in the range FA $\in$ [25–62]°. As a result, FA = 25° was chosen to maintain a reasonable FWHM and signal level ($>$ 90 %, see 2D-#2 in Table 2) inside the cylinder.

A slab profile measured in vivo (Fig. 2d) is illustrated in Figure 2e (occipital cortex, ZY orientation). As in Figure 2c, the MR signal originated mainly from the cylinder. In a plane transversal to the cylinder axis (see plain line in Fig. 2e), the excitation pattern (Fig. 2f, circles) closely matched the ideal profile (dotted line, Gaussian distribution, $FWHM_{sim} = 2*r_0 = 14$ mm). The nine directions of interest (three physical axes, six side-diagonals of the cube) were tested and showed very similar profiles. Only one direction is illustrated in the figure for clarity. The 2D-RF pulses present good spatial selectivity and very little residual excitation.

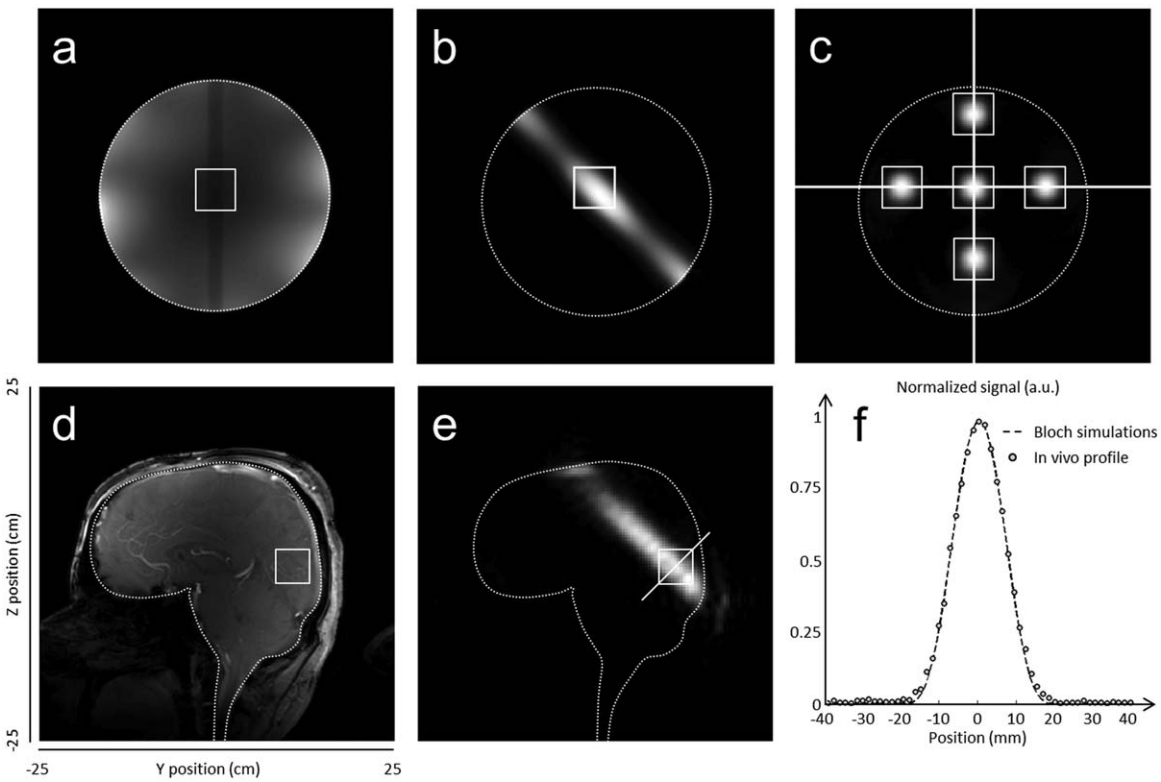

FIG. 2. Positions of the acetate phantom (**a**) and brain (**d**) used for characterization of the gradient system and experimental profile. In both images the white box represents the 25 × 25 × 25 mm^3 shimming volume. **b–e:** Cylindrical excitation ($r_0 = 0.7$ cm) along the YZ direction (GE-3D, FOV 20 × 20 cm^2, sagittal view) near the phantom isocenter (**b**) and the occipital cortex (**e**) (sagittal view extracted from a 3D dataset, arbitrary units). **c:** Accuracy of gradient system calibration. The five excitation locations (± 0/50 mm off-center in X/Y direction) closely matched the designed positions (white boxes). The solid white lines indicate the axes centers. In all images the dotted circles delineate the edges of the phantom/brain. **f:** In-plane characterization (res. 1.5 mm) of the cylinder illustrated in **e** (occipital cortex, YZ orientation). The experimental in vivo profile across the slab (circles) closely matches the simulated data (dotted line).

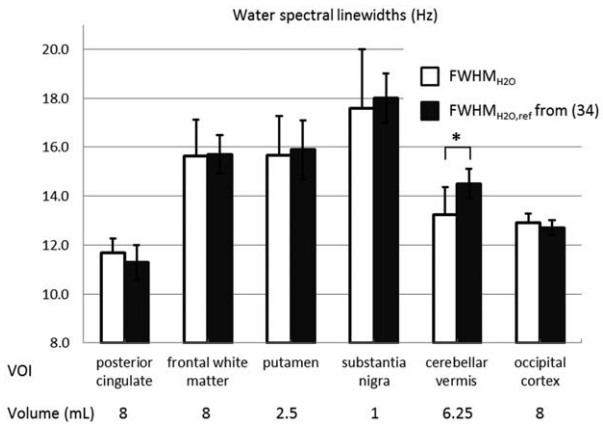

FIG. 3. Water spectral linewidth (in Hz) obtained in vivo after localized shimming using multidimensional excitation pulses and reference values from (34). *indicates that the two distributions are significantly different ($P < 0.05$). The error bars represent standard deviations across subjects (N = 7 and 14, respectively).

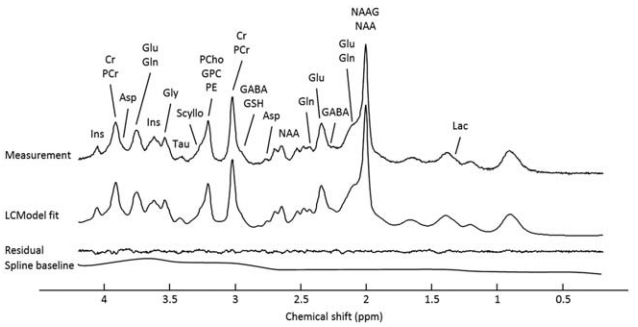

FIG. 4. Proton spectrum acquired after localized shimming including 2D-RF slab excitation and LCModel fitting. Spectra were obtained from an 8 mL cubic VOI in the posterior cingulate.

Water Spectral Linewidth

After localized shimming, the $FWHM_{H2O}$ obtained in the occipital cortex were in the range [12.5–13.4] Hz, in agreement with values reported at 7T (1,34,37). There was no statistical difference (N = 7, $P > 0.5$) between the water spectral linewidths obtained, when using either 2D-RF excitation or adiabatic RF pulses.

The fast 2D-RF shimming protocol was applied to five additional brain regions (N = 7). As seen in Figure 3, the $FWHM_{H2O}$ were in very close agreement with the values reported by Emir et al (34). Water spectral linewidths were only found significantly different ($P < 0.05$) in the cerebellum, where our measurements (13.2 ± 1.1 Hz) were somewhat smaller than the value reported in (34) (14.5 ± 0.6 Hz).

Neurochemical Profile

Narrow water linewidths constitute at high field a good indicator that a large number of brain metabolites can be properly identified and that their concentration can be quantified with precision using MRS. The spectrum of Figure 4 was acquired after localized shimming in the posterior cingulate. The quality of the spectrum and fitting is characterized by efficient water suppression, absence of lipid contamination and very little residual fitting and flat spline baseline. A large number of metabolites were identified and quantified according to well established criteria (15 metabolites with CRLB < 20%, see Table 3), in agreement with other MRS studies at 7T using short acquisition times (29).

DISCUSSION AND CONCLUSIONS

The present study shows that efficient localized shimming at high field using projection mapping with 2D-RF pulses is possible. The spectral linewidths obtained in various brain regions were as narrow as those obtained using conventional projection mapping with adiabatic RF pulses (10) and B_1 shimming (34). Compared with the SE implementation, the GE method using 2D-RF pulses deposited far less RF energy (0.1%) and allowed to decrease TR and the total shim time (−83%) with equal performance.

In practice, the shimming volume needs to be larger than the VOI to perform efficient OVS, WS and to quantify brain metabolites with precision. Choosing a slab thickness of $r_0 = 0.7$ cm provided an suitable trade-off between NMR signal and RF pulse duration (5 ms) for conventional VOI sizes in MRS (34,37). For larger VOIs, the pulse duration can be shortened, making the excitation pattern more robust to B_0 variations. The pulse shape, directly derived from the Fourier theorem, does not require knowledge of the magnetic field distribution. Although better excitation patterns can be designed using B_0 and B_1 maps, field map acquisitions would prolong the total execution time for adjustment of the shims. Using an iterative shimming method makes the exact fidelity of the excitation profile less important, and fast B_0 mapping can be achieved using simple numerical tools and minimal RF energy deposition.

B_0 variations can distort the ideally cylindrical excitation pattern because of the long RF pulse duration (14,15). At 7T and for a 5-ms pulse, moderate blurring of the profile is expected for small B_0 perturbations (0–1 ppm). However, larger frequency offsets can lead to severe signal reduction, spatial distortions and unwanted

Table 3
Cramer Rao Lower Bound (%) and Concentration (mmol.kg^{-1}) of Different Metabolites[a]

Metabolite	CRLB (%)	Conc. (mmol.kg^{-1})
Asp	8	3.5
PCho	19	0.6
Cr + PCr	1	8.0
GABA	11	1.3
Gln	4	3.8
Glu	2	11.9
GSH	6	1.4
Gly	37	0.3
Ins	2	5.9
Lac	13	0.6
NAA	1	12.9
Scyllo	30	0.1
Tau	6	2.2
NAAG	8	1.3
GPC	13	0.9
PE	9	1.7

[a]Metabolite concentrations were scaled to a total Cr of 8 mmol.kg^{-1}.

excitation that affect the selection profile (14) and thus the convergence of the algorithm. This problem was minimized by performing global shimming before the localized technique.

When exciting at the water frequency, lipids will experience strong off-resonance effects around 3.3 to 3.5 ppm (43) during the RF excitation. Unwanted excitation can occur on the edges of the brain and add to the total MR signal of the projection. This situation can be mitigated by using presaturation of the unwanted resonances when the convergence of the shimming algorithm is hindered. One case of moderate fat contribution to the water signal (< 10 %) was observed in this study, however, without any effect on the shimming efficiency.

In the absence of B_1 shimming, adiabatic RF pulse durations must be kept long enough so that the whole brain area can be covered with sufficiently high efficiency. This is particularly true for the very energetic inversion pulses that are used to refocus the magnetization along thin slabs, and that must remain below hardware power constraints. Those limitations directly impact the resulting SAR and, indirectly, the total acquisition time of the sequence. Depending on the subject, the minimum available TR varied between 2600 and 3800 ms for a single iteration of the adiabatic implementation of FASTMAP/FASTESTMAP. The adiabatic RF pulses used in this study (hyperbolic secant, HS8) were not SAR-optimized. Given the tremendous SAR reduction (−99 %) compared with HS8, 2D-RF pulses are expected to deposit far less energy than any combination of five "low-SAR adiabatic RF pulses" (including four inversion pulses).

As previously shown (9), adiabatic RF pulses are not necessary for the convergence of the shimming algorithm. More generally, during a spectroscopic experiment a step is to determine the local B_1 inside the VOI to counteract the intrinsic low SNR in MRS and achieve efficient OVS and WS (13,29). This is usually performed by adjusting the voltage sent during MR acquisition and maximizing the received signal. Adjusting the flip angle also ensures sufficient signal during the shimming process. Nevertheless, adiabatic pulses perform better in locations with poor B_1 coverage, at the expense of increased SAR. This impact on SAR is magnified due to the nonlinear phase accumulated during adiabatic refocusing pulses, which need to be used in pairs. Here the MR signal from the excited slab is directly refocused using MR gradients and a single low-amplitude 2D-RF pulse replaces five SAR-intensive pulses.

In this study, we were unable to detect any difference in terms of step-wise convergence of the iterative shimming algorithm, as evidenced by the equivalent MR signal level reached by the two techniques. After further maximization of the SNR per unit time (TR = 125 ms, NA = 4, FA = 15°), dynamic monitoring of the shim changes found by the algorithm after each step suggested that the protocol can be further optimized by reducing the number of iterations before the second-order shims adjustments. Efficient shimming requires for instance less than 24 s in the occipital lobe or posterior cingulate. In general, the total execution time suffers very little from additional steps (+3/6 s per iteration), making the protocol all the more suitable for in vivo studies.

The main interest of using 2D-RF pulses relies in the increased speed of the resulting shimming protocol. This assumption is valid when TR is constrained due to SAR limitations and/or spin relaxation considerations. In practice, this phenomenon only appears when performing MRI/MRS at ultrahigh field (> 3T). At lower field, T_1 is smaller and the energy deposited by the RF pulses does not restrict the use of small TRs. Both techniques are then equivalent and converge rapidly to optimal shim values.

One could also consider the benefit of 2D-RF localized shimming compared with a nonadiabatic SE implementation of FASTMAP or FASTESTMAP. While a nonadiabatic SE sequence would deposit less RF energy than the full adiabatic sequence (rSAR in the range [3–16] % using conventional RF pulses, depending on their durations), it could fail to provide a strong and clean localized MR signal at small repetition times (125–500 ms) due to partial T_1 relaxation after spin inversion. This does not affect 2D-RF pulses, that can also benefit from shorter TR through increase of the SNR per unit time when used in the small tip angle regime.

Our 2D-RF pulses were found insensitive to small motion and performed well toward the upper end of the small tip angle regime. In addition, the RF amplifier and gradient system (including pre-emphasis unit) performed robustly and ensured reproducibility and reliability of the results. Should that not be the case, various techniques have been developed to compensate for distorted k-space trajectories, correct for eddy currents and calibrate the gradient system (27,44–46). Most of these techniques only require a single calibration, so that reliable k-space spiral trajectories can still be rapidly generated once this process is done.

Notably, localized shimming combined with multidimensional pulses converged in less than a minute in almost all brain regions tested. The protocol detailed in this work only failed in the pons, with both RF pulse implementations. Near this location, dedicated passive intra-oral shimming (47) and B_1 shimming (34) might be needed to compensate for the extremely poor and inhomogeneous B_0 and B_1 coverage, respectively.

We chose to focus here on localized shimming on small volumes, where B_1 can be considered homogeneous. However, adiabatic pulses can still remain a better choice when the VOI is large and includes one or several signal drop-out areas. The 3D B_0 mapping techniques perform also well for full brain shimming, and limitations mainly arise from the number of spherical harmonic orders that can be tuned with an available set of shim coils.

We conclude that the technique introduced in this study constitutes a fast low-SAR alternative to conventional projection mapping using adiabatic RF pulses. The 2D-RF pulses provide sufficient selectivity to rapidly map the local B_0 in vivo and iteratively converge toward the optimal shim settings.

ACKNOWLEDGMENTS

The authors declare no conflict of interest. This work was supported by the Centre d'Imagerie Bio-Médicale (CIBM) of the University of Lausanne (UNIL), the Swiss

Federal Institute of Technology Lausanne (EPFL), the University of Geneva (UniGe), the Centre Hospitalier Universitaire Vaudois (CHUV), the Hôpitaux Universitaires de Genève (HUG) and the Leenaards and the Jeantet Foundations and by a Swiss National Science grant to R. Gruetter. The authors thank Ralf Mekle (PTB, Berlin) and Eddie Auerbach (CMRR, Minneapolis) for stimulating discussions and vital assistance in implementing the dynamic update of the shims.

REFERENCES

1. Mekle R, Mlynarik V, Gambarota G, Hergt M, Krueger G, Gruetter R. MR spectroscopy of the human brain with enhanced signal intensity at ultrashort echo times on a clinical platform at 3T and 7T. Magn Reson Med 2009;61:1279–1285.
2. Mlynarik V, Cudalbu C, Xin L, Gruetter R. 1H NMR spectroscopy of rat brain in vivo at 14.1Tesla: improvements in quantification of the neurochemical profile. J Magn Reson 2008;194:163–168.
3. Koch KM, Rothman DL, de Graaf RA. Optimization of static magnetic field homogeneity in the human and animal brain in vivo. Prog Nucl Magn Reson Spectrosc 2009;54:69–96.
4. Romeo F, Hoult DI. Magnet field profiling: analysis and correcting coil design. Magn Reson Med 1984;1:44–65.
5. Hetherington HP, Chu WJ, Gonen O, Pan JW. Robust fully automated shimming of the human brain for high-field 1H spectroscopic imaging. Magn Reson Med 2006;56:26–33.
6. Miyasaka N, Takahashi K, Hetherington HP. Fully automated shim mapping method for spectroscopic imaging of the mouse brain at 9.4 T. Magn Reson Med 2006;55:198–202.
7. Schneider E, Glover G. Rapid in vivo proton shimming. Magn Reson Med 1991;18:335–347.
8. Gruetter R. Automatic, localized in vivo adjustment of all first- and second-order shim coils. Magn Reson Med 1993;29:804–811.
9. Gruetter R, Boesch C. Fast, noniterative shimming of spatially localized signals. In vivo analysis of the magnetic field along axes. J Magn Reson 1992;96:323–334.
10. Gruetter R, Tkac I. Field mapping without reference scan using asymmetric echo-planar techniques. Magn Reson Med 2000;43:319–323.
11. Shen J, Rycyna RE, Rothman DL. Improvements on an in vivo automatic shimming method [FASTERMAP]. Magn Reson Med 1997;38: 834–839.
12. Shen J, Rothman DL, Hetherington HP, Pan JW. Linear projection method for automatic slice shimming. Magn Reson Med 1999;42: 1082–1088.
13. Tkac I, Gruetter R. Methodology of 1H NMR spectroscopy of the human brain at very high magnetic fields. Appl Magn Reson 2005;29: 139–157.
14. Qian Y, Zhao T, Hue Y-K, Ibrahim TS, Boada FE. High-resolution spiral imaging on a whole-body 7T scanner with minimized image blurring. Magn Reson Med 2010;63:543–552.
15. Yudilevich E, Stark H. Spiral sampling in magnetic resonance imaging-the effect of inhomogeneities. IEEE Trans Med Imaging 1987; 6:337–345.
16. Block KT, Frahm J. Spiral imaging: a critical appraisal. J Magn Reson Imaging 2005;21:657–668.
17. Delattre BMA, Heidemann RM, Crowe LA, Vallée J-P, Hyacinthe J-N. Spiral demystified. Magn Reson Imaging 2010;28:862–881.
18. Nehrke K, Bornert P, Groen J, Smink J, Bock JC. On the performance and accuracy of 2D navigator pulses. Magn Reson Imaging 1999;17: 1173–1181.
19. Smith TB, Nayak KS. Reduced field of view MRI with rapid, B1-robust outer volume suppression. Magn Reson Med 2012;67:1316–1323.
20. Zhao T, Qian Y, Hue Y-K, Ibrahim TS, Boada F. An improved analytical solution for variable density spiral design. In Proceedings of the 16th Annual Meeting of ISMRM, Toronto, Canada, 2008. Abstract 1342.
21. Glover GH. Simple analytic spiral K-space algorithm. Magn Reson Med 1999;42:412–415.
22. Ahn CB, Kim JH, Cho ZH. High-speed spiral-scan echo planar NMR imaging-I. IEEE Trans Med Imaging 1986;5:2–7.
23. Pauly J, Nishimura D, Macovski A. A k-space analysis of small-tip-angle excitation. J Magn Reson 1989;81:43–56.
24. Pauly J, Nishimura D, Macovski A. A linear class of large-tip-angle selective excitation pulses. J Magn Reson 1989;82:571–587.
25. Marques JP, Kober T, Krueger G, van der Zwaag W, Van de Moortele PF, Gruetter R. MP2RAGE, a self bias-field corrected sequence for improved segmentation and T1-mapping at high field. Neuroimage 2010;49:1271–1281.
26. Davies NP, Jezzard P. Calibration of gradient propagation delays for accurate two-dimensional radiofrequency pulses. Magn Reson Med 2005;53:231–236.
27. Robison RK, Devaraj A, Pipe JG. Fast, simple gradient delay estimation for spiral MRI. Magn Reson Med 2010;63:1683–1690.
28. Pauly J, Le Roux P, Nishimura D, Macovski A. Parameter relations for the Shinnar-Le Roux selective excitation pulse design algorithm [NMR imaging]. IEEE Trans Med Imaging 1991;10:53–65.
29. Schaller B, Mekle R, Xin L, Kunz N, Gruetter R. Net increase of lactate and glutamate concentration in activated human visual cortex detected with magnetic resonance spectroscopy at 7 tesla. J Neurosci Res 2013;91:1076–1083.
30. Snaar JE, Teeuwisse WM, Versluis MJ, van Buchem MA, Kan HE, Smith NB, Webb AG. Improvements in high-field localized MRS of the medial temporal lobe in humans using new deformable high-dielectric materials. NMR Biomed 2011;24:873–879.
31. Teeuwisse WM, Brink WM, Webb AG. Quantitative assessment of the effects of high-permittivity pads in 7 Tesla MRI of the brain. Magn Reson Med 2012;67:1285–1293.
32. Eggenschwiler F, Kober T, Magill AW, Gruetter R, Marques JP. SA2RAGE: a new sequence for fast B1+ -mapping. Magn Reson Med 2012; 67:1609–1619.
33. Frahm J, Bruhn H, Gyngell ML, Merboldt KD, Hanicke W, Sauter R. Localized high-resolution proton NMR spectroscopy using stimulated echoes: initial applications to human brain in vivo. Magn Reson Med 1989;9:79–93.
34. Emir UE, Auerbach EJ, Van De Moortele PF, Marjanska M, Ugurbil K, Terpstra M, Tkac I, Oz G. Regional neurochemical profiles in the human brain measured by (1)H MRS at 7 T using local B(1) shimming. NMR Biomed 2012;25:152–160.
35. Mangia S, Tkac I, Gruetter R, Van de Moortele PF, Maraviglia B, Ugurbil K. Sustained neuronal activation raises oxidative metabolism to a new steady-state level: evidence from 1H NMR spectroscopy in the human visual cortex. J Cereb Blood Flow Metab 2007;27:1055–1063.
36. Tkac I, Andersen P, Adriany G, Merkle H, Ugurbil K, Gruetter R. In vivo 1H NMR spectroscopy of the human brain at 7 T. Magn Reson Med 2001;46:451–456.
37. Tkac I, Oz G, Adriany G, Ugurbil K, Gruetter R. In vivo 1H NMR spectroscopy of the human brain at high magnetic fields: metabolite quantification at 4T vs. 7T. Magn Reson Med 2009;62:868–879.
38. Xin L, Schaller B, Mlynarik V, Lu H, Gruetter R. Proton T1 relaxation times of metabolites in human occipital white and gray matter at 7 T. Magn Reson Med 2013;69:931–936.
39. Provencher SW. Estimation of metabolite concentrations from localized in vivo proton NMR spectra. Magn Reson Med 1993;30:672–679.
40. Govindaraju V, Young K, Maudsley AA. Proton NMR chemical shifts and coupling constants for brain metabolites. NMR Biomed 2000;13: 129–153.
41. Xin L, Gambarota G, Mlynarik V, Gruetter R. Proton T2 relaxation time of J-coupled cerebral metabolites in rat brain at 9.4 T. NMR Biomed 2008;21:396–401.
42. Mlynarik V, Gambarota G, Xin L, Gruetter R. Precision of metabolite concentrations obtained by LCModel as a function of the signal-to-noise ratio in rodent brain. In Proceedings of the 15th Annual Meeting of ISMRM, Berlin, Germany, 2007. Abstract 3173.
43. Haacke EM, Brown RW, Thompson MR, Venkatesan R. Magnetic resonance imaging: physical principles and sequence design. NY: John Wiley and Sons; 1999.
44. Addy NO, Wu HH, Nishimura DG. Simple method for MR gradient system characterization and k-space trajectory estimation. Magn Reson Med 2012;68:120–129.
45. Duyn JH, Yang Y, Frank JA, van der Veen JW. Simple correction method fork-space trajectory deviations in MRI. J Magn Reson 1998; 132:150–153.
46. Tan H, Meyer CH. Estimation of k-space trajectories in spiral MRI. Magn Reson Med 2009;61:1396–1404.
47. Wilson JL, Jenkinson M, Jezzard P. Protocol to determine the optimal intraoral passive shim for minimisation of susceptibility artifact in human inferior frontal cortex. Neuroimage 2003;19:1802–1811.